Published in final edited form as:

*IEEE Trans Med Imaging*. 2005 July ; 24(7): 868–877.

# Evaluation of Fully 3-D Emission Mammotomography With a Compact Cadmium Zinc Telluride Detector

**Caryl N. Brzymialkiewicz, Member, IEEE**,
Multi-Modality Imaging Laboratory, Departments of Biomedical Engineering and Radiology, Duke University Medical Center, DUMC-3949, Durham NC 27710 USA

**Martin P. Tornai, Member IEEE**,
Multi-Modality Imaging Laboratory, Departments of Biomedical Engineering and Radiology, Duke University Medical Center, Durham NC 27710 USA

**Randolph L. McKinley, Member IEEE**, and
Multi-Modality Imaging Laboratory, Departments of Biomedical Engineering and Radiology, Duke University Medical Center, Durham NC 27710 USA

**James E. Bowsher, Member IEEE**
Department of Radiology, Duke University Medical Center, Durham, NC 27710 USA

Caryl N. Brzymialkiewicz: cnb3@duke.edu

## Abstract

A compact, dedicated cadmium zinc telluride (CZT) gamma camera coupled with a fully three-dimensional (3-D) acquisition system may serve as a secondary diagnostic tool for volumetric molecular imaging of breast cancers, particularly in cases when mammographic findings are inconclusive. The developed emission mammotomography system comprises a medium field-of-view, quantized CZT detector and 3-D positioning gantry. The intrinsic energy resolution, sensitivity and spatial resolution of the detector are evaluated with Tc-99m (140 keV) filled flood sources, capillary line sources, and a 3-D frequency-resolution phantom. To mimic realistic human pendant, uncompressed breast imaging, two different phantom shapes of an average sized breast, and three different lesion diameters are imaged to evaluate the system for 3-D mammotomography. Acquisition orbits not possible with conventional emission, or transmission, systems are designed to optimize the viewable breast volume while improving sampling of the breast and anterior chest wall. Complications in camera positioning about the patient necessitate a compromise in these two orbit design criteria. Image quality is evaluated with signal-to-noise ratios and contrasts of the lesions, both with and without additional torso phantom background. Reconstructed results indicate that 3-D mammotomography, incorporating a compact CZT detector, is a promising, dedicated breast imaging technique for visualization of tumors <1 cm in diameter. Additionally, there are no outstanding trajectories that consistently yield optimized quantitative lesion imaging parameters. Qualitatively, imaging breasts with realistic torso backgrounds (out-of-field activity) substantially alters image characteristics and breast



Correspondence to: Caryl N. Brzymialkiewicz, cnb3@duke.edu.

morphology unless orbits which improve sampling are utilized. In practice, the sampling requirement may be less strict than initially anticipated.

**Index Terms**

Breast imaging; CZT detector; emission imaging; mammotomography; single photon emission computed tomography; SPECT; three-dimensional orbits

## I. Introduction

COMPACT, dedicated gamma cameras coupled with a fully three-dimensional (3-D) acquisition system can serve as a secondary diagnostic tool for imaging of breast cancers, particularly in cases when mammographic findings are inconclusive. The significance of a compact camera in single photon emission imaging is its ability to facilitate closer proximity imaging, thus minimizing distance-dependent spatial resolution limitations. An advantage of employing nuclear medicine techniques stems from the fact that the accuracy of scintimammography is unaffected by breast density: studies have shown women with dense breasts may benefit most from this complementary imaging technique [1], [2]. Thus, several groups have investigated compact position-sensitive photomultiplier tube (PSPMT)-based gamma cameras for the breast imaging paradigm [3]–[6].

Compared to planar imaging alone, there is a significant increase in the accuracy of breast imaging for the diagnosis of primary breast cancer when mammography and scintimammography are combined [7]. Diagnostic accuracy may be further improved when using tomography rather than a simple combination of scintimammography and mammography, given that contrast improves with such a 3-D technique. In addition, the 3-D localization of the tumor is provided, as is the potential for *in vivo* quantification of lesion activity. Single photon emission computed tomography (SPECT) specifically for breast imaging has been investigated both with clinical gamma cameras [8]–[17] and dedicated systems [4], [17]–[22]. Our group has previously demonstrated that a compact, fully 3-D hemispherical positioning gantry that allows for imaging with a detector positioned anywhere about a pendant, uncompressed breast phantom significantly improves image quality and lesion visualization [20], [21]. Those studies were performed with quantized NaI(Tl) scintillator, PSPMT-based compact gamma cameras.

While these dedicated PSPMT cameras offer an improvement over clinical gamma cameras, the energy discrimination can be further improved by using cadmium zinc telluride (CZT) semiconductor detectors. The use of CZT detectors for the detection of breast lesions has been previously proposed and investigated through SPECT simulation studies [22] and preprototype measurements [18], and scintimammography measurements [23]. Solid-state detectors made of CZT boast a markedly improved energy resolution over scintillator-based NaI(Tl), with reported measurements of 4%–7% full-width at half-maximum (FWHM) at 140.6 keV [23]–[27], as compared to NaI(Tl)'s typical energy resolution of 9%–10% [28]. Indeed, for compact gamma cameras utilizing quantized elements, the energy resolution, and hence scatter rejection, is usually poorer still. Scintimammography phantom imaging studies indicate that scatter from cardiac and hepatic background can significantly contaminate the

primary lesion signal [29]. While it is generally accepted that better energy resolution performance yields improved emission image quality, it is unclear what specific effect this will have in the 3-D breast imaging paradigm [20], [21].

Using a fully 3-D acquisition geometry discussed here, there is an infinite set of camera trajectories, or orbits, with which to acquire projection data. The camera motions and techniques presented here can also directly be applied to other imaging modalities, such as cone-beam X-ray transmission imaging. The gantry's several degrees of freedom allow any detector, source/detector or even detector/detector connected to it to be positioned anywhere about a $2\pi$ steradian solid angle of coverage. For example, by replacing the gamma camera utilized here with a flat-panel digital X-ray detector, combined with an opposing X-ray tube, cone-beam transmission acquisitions of a pendant breast phantom can be performed [30], [31].

While a simple, vertical-axis-of-rotation orbit for an emission imaging camera [13] with a parallel-hole collimator yields a completely sampled volume [32], [33], the imaged breast volume, for example, is smaller than for an acquisition orbit which includes camera tilt. Due to positioning restraints imposed by the detector, the furthest into the breast one can image without tilt is limited to the plane perpendicular to the nipple-chest axis where the camera is adjacent to the torso. Cameras with a large dead edge further decrease the viewable breast volume. One main advantage of fully 3-D orbits that utilize increased polar tilt is an increased viewable breast volume, potentially into the chest wall region [20]. However, with increased tilt angle, the camera may directly view cardiac and hepatic regions that take up the injected radiopharmaceutical, which could contribute primary background contamination to the 2-D projection images of the breast.

Using a compact CZT detector to image lesions in a uniform breast background, the primary aim of this study is to evaluate the imaging ability of the developed emission mammotomography system, both with and without additional torso backgrounds, with some previously investigated and newer trajectories. To our knowledge, this is the first implementation and evaluation of a fully developed CZT detector and system for dedicated tomographic imaging of the breast (mammotomography).

## II. Planar and SPECT Performance Characteristics of the CZT Detector

### A. Methods

The commercially available, production LumaGEM™ 3200-S camera (*Gamma Medica Inc.*, Northridge, CA) (Fig. 1) utilizes a 60 × 84 array of 2.5 × 2.5 × 6 $mm^3$ quantized CZT elements. The detector is kept at 15 °C, using water cooling. We evaluated the camera with an unmatched parallel beam, lead collimator with hexagonally arranged holes (1.22-mm hole size flat-to-flat, 0.2-mm septa, 25.4-mm height).

With the collimator removed, the intrinsic energy resolution was measured for 10 M total counts using a point source of Tc-99m located approximately 1 m from the camera surface. Count rates were ~17.5 kcps using an open energy window (~10 kcps in a 16% symmetric (±8%) window about the photopeak). Sensitivity, defined as (counts/sec)/mCi, was

measured with a 14-cm-diameter petri dish filled with an ~3-mm layer of 2.6 mCi of Tc-99m, placed 10 cm from the collimator face. Counts were recorded for 60 s. The dose calibrator in our lab has a ±5% error. The sensitivity measurement is based on a 16% symmetric (±8%) energy window about the 140-keV photopeak, which is the window size used for all of the studies performed to characterize the detector (all those found in Section II). Energy windows are applied globally to all pixels, i.e., there is not a separate energy window for each discrete pixel, though in principle there could be.

Planar spatial resolution was measured by acquiring images of a single capillary tube in air, filled with 3.8 mCi of Tc-99m in 6.0 cm of its length. Projection data were acquired with the line source moved across the detector face both horizontally and vertically with respect to the camera, in 1-mm increments for a total of 10 mm. For both the horizontal and vertical directions, the tube was then placed at the position yielding the lowest FWHM, and projection data were acquired at a collimator-to-source distance of 1 through 10 cm. The expected system spatial resolution is a function of the intrinsic and collimator resolutions. Collimator resolution ($R_{coll}$) was calculated by $R_{coll} = [d(l_{eff} + b + c)]/l_{eff}$, where $d$ is the hole diameter, $l_{eff}$ is the 'effective length' of the collimator holes, $b$ is the distance from the collimator to the radiation source, and $c$ is the collimator-to-detector distance [34], [35]. The effective collimator length is calculated by $l_{eff} = l - 2\mu^{-1}$, where $l$ is the length of the holes and $\mu$ is the linear attenuation coefficient of the collimator material (lead) [34].

Reconstructed spatial resolution was determined from SPECT measurements of two capillary tubes in air, one filled with 3.8 mCi of Tc-99m in 6.0 cm of its length, the other filled with 1.8 mCi of Tc-99m in 3.0 cm, both suspended along the vertical axis of rotation with one placed on the axis of rotation and one offset by 2 cm. Simple circular tomography over 360° was used for these measurements with 128 projections, at 5 s/projection. Acquisitions were made at 3-, 5-, and 7-cm rotation radii. Note that the radius-of-rotation (ROR) is defined as the perpendicular distance from the center of the detector face, at the front face of the collimator, to the center-of-rotation (COR). Images were reconstructed from projection data using an ordered subsets expectation maximization (OSEM) algorithm [36], [37] implemented with a ray-tracing capability, using 8 subsets, 5 iterations, and 2.5-mm grid voxels. Since spatial resolution was not modeled within these reconstructions, there is a limit to how much spatial resolution the reconstructions can recover, and that limit will be reached within a relatively small number of iterations. The number of subsets was chosen based on previous evaluations of tradeoffs between signal-to-noise ratio (SNR) and contrast of small lesions [20], [21].

A 7.7-cm diameter cylinder containing a resolution-frequency phantom consisting of acrylic mini-rods each 2.6 cm long (model ECT/DLX/MP, *Data Spectrum Corp.*, Hills-borough, NC) was used as another measure of the tomographic spatial resolution of the system (Fig. 2). In each of six sectors, the rods had equal diameters of 4.7, 3.9, 3.1, 2.3, 1.5, and 1.1 mm, spaced on twice their diameter. Water containing 15.6 mCi of Tc-99m filled the interstitial spaces between the rods, thus, images are of "cold" rods. The phantom was oriented such that the rods were vertical, parallel to the axis of rotation. The camera and phantom were both leveled, and the rods were placed in the central portion of the field of view (FOV). The ROR was fixed at 4.4 cm. The 16% energy window yielded count rates of ~5.9 kcps. Simple

circular tomography was used for these measurements with 256 projections over 360° and an acquisition time of 28 s/projection.

### B. Results

Of the detector's 5120 pixels, 99.8% were routinely usable. The dead pixels were randomly dispersed throughout the imaging FOV, with only one bad 4-pixel cluster at the edge of the distal FOV. The system has a dead-pixel correction scheme supplied by the manufacturer, which includes a linear interpolation of the surrounding pixels' values. For our imaging studies, the phantoms did not extend into that portion of the detector. One might expect a similar dead pixel fraction and random distribution from similar imaging devices. Furthermore, extensive quality control studies are performed before each set of experiments; should excessive dead pixels appear to be concentrated in any one region, the modules could be replaced within the camera. The measured uniformity of the detector was ±4.0%, given as the overall standard deviation of all pixels divided by the global mean.

The gain balanced, summed energy spectra (Fig. 3) yielded an intrinsic energy resolution of 6.8% FWHM at 140 keV. Using the same protocol for calculation of the FWHM (as per [38]) for each individual pixel resulted in a mean intrinsic energy resolution of 6.7%, with a range of 3.5% to 24.8% (Fig. 3, histogram). The measured sensitivity of the system for the parallel-beam collimator using Tc-99m was 1402 cps/mCi (37.9 cps/MBq).

Average planar spatial resolution FWHM and full-width-tenth-maximum (FWTM) values as measured with the capillary line source, according to [38], for collimator-source distances of 1 and 10 cm are shown in Table I. Planar spatial resolution plotted as a function of distance to the detector compared well to the calculated system resolution (Fig. 4). Horizontal and vertical measurements may be different due to the line source being ideally aligned with the collimator holes in one case, and/or nonalignment with the Cartesian distribution of the quantized CZT elements. Furthermore, the size and shape of the collimator holes are not matched to the detector elements, and the collimator holes are not aligned with the Cartesian distribution of the square pixels. The system's current unmatched collimator can potentially introduce aliasing and sensitivity fluctuations across an individual detector element. While some groups are investigating un/matched collimator designs for pixellated detectors [39]–[41], it is known that rotating the unmatched collimator with respect to the detector pixels would reduce these effects [42].

SPECT spatial resolution results are shown in Fig. 5 for the fifth iteration data, where 10-pixel-wide profiles were drawn in both the coronal and sagittal slices, and Gaussian curves were fit to the profiles to extract the FWHM information. Resolution measurements are not significantly different with fewer iterations.

Reconstructed results with 8 subsets, 20 iterations, and 2.5-mm voxels, from the mini-rod measurements are shown in Fig. 2. The second sector of rods (3.9-mm diameter) are clearly distinguishable, as would be expected with results from Figs. 4, and 5 given the ROR of 4.4 cm. The 3.1-mm rods are also discernible; though the profile reveals a relatively low contrast, the rods can indeed be resolved.

## III. Three-Dimensional Mammotomography

The significance of any 3-D orbit with a dedicated breast imaging system is that it allows for fully 3-D imaging of an uncompressed, pendant breast while avoiding physical features or other hindrances from a patient during the acquisition. The tomographic gantry (Fig. 6) used to position the camera's central ray at any point in a hemisphere about the COR has been previously described [20], [21]. A basis set of orbits was initially characterized using a smaller, 12.8 × 12.8 $cm^2$ FOV NaI(Tl) camera incorporated onto the dedicated emission mammotomograph [21]. While results showed significant improvements in contrasts and SNRs for breast lesions as compared to simple vertical-axis-of-rotation acquisitions and uncompressed planar imaging, the system was limited by the relatively small FOV. Image artifacts resulted from a necessary camera shift to compensate for large, truncated breast volumes.

The new CZT detector used here has a larger FOV and obviates this camera shift of our previous work. Thus, in this work, we evaluate a subset of orbits from [21] here acquired with the full FOV CZT detector. In addition, we evaluate newer orbits. Ideally, an acquisition orbit should: 1) meet Orlov's sampling criterion for sufficient data collection for accurate reconstruction of the activity distribution within the breast when the activity is fully within the camera's FOV for each projection angle [32]; 2) maximize the viewable breast volume; 3) minimize the background contamination from cardiac and hepatic sources; and 4) contour the breast to minimize the distance related resolution degradations.

If used as a secondary diagnostic tool, the emission mammotomography system evaluated here can image an indeterminate lesion which may have presented on an initial mammogram. Orbits can be designed to contour the breast keeping the detector position near such a lesion. Thus, for this set of experiments, we examine those orbits illustrated in Fig. 7(a). Given the geometry of a pendant breast and the tilts afforded by the system to contour the breast, proximity of different parts of the camera will vary with respect to the breast and an azimuthal axis of rotation. Orbits are designed to optimally contour the breast utilizing dynamic ROR control [example given in Fig. 7(b)], allowing at most a 1-cm separation between the camera's center and the breast phantom surface.

While this paper focuses on parallel-beam imaging utilizing a focal spot at infinity, Orlov's sampling criteria have been shown to be a special case [33] of Tuy's condition for cone-beam sampling [43], which outlines criteria for cone-beam type geometries that are also possible with our system. The flexibility of the gantry allows for investigation of various sampling schemes, for a variety of converging or even diverging collimation beam configurations.

### A. Methods

Two acrylic lesions, one 8-mm and one 5-mm inner diameter with ~1-mm wall thickness (*Data Spectrum Corp*.) were inserted into a ~935 ml custom fabricated, fillable anthropomorphic breast phantom (*Radiology Support Devices Inc*., Newport Beach, CA) as shown in Fig. 8. The 8-mm lesion was placed centrally in the breast, while the 5-mm lesion was placed proximally. The custom-made breast phantom is one of several, each with

varying sizes and shapes; this particular model has dimensions given in Table II. The dimensions of these phantoms are within the ranges measured clinically [44]. Specific orbit parameters used for these acquisitions, including ROR ranges, are given in Table III. The lesion:breast radionuclide concentration ratio was 9.8:1, with an absolute lesion activity concentration of 12.1 $\mu$Ci/ml. The initial scan was acquired for 20 min, with subsequent acquisitions adjusted to compensate for radioactive decay. As in Section II, a ±8% symmetric energy window about the 140-keV photopeak was used, yielding count rates of ~0.9 kcps. The breast phantom was attached to the anthropomorphic torso phantom to simulate complications in patient positioning, but the torso was *not* filled with radioactivity.

To more nearly simulate a clinical study and, thus, match the biodistribution of activity in a patient, an anthropomorphic torso phantom containing a heart, liver, and lungs (*Radiology Support Devices Inc*.) was filled according to compiled, published data [3], [4], [45]–[47]. The ~1060 ml breast phantom, torso and organs were filled according to the concentration ratios given in Table IV, assuming an initial total dose of 25 mCi (925 MBq), with the heart uptake of 1.2% after 5 min [47]. Two lesions, one 9.5-mm and one 8.0-mm inner diameter with ~1-mm wall thickness (*Data Spectrum Corp.*) were also filled according to the concentration ratios given in Table IV. The 9.5-mm lesion was placed centrally in the breast, while the 8-mm lesion was placed in the upper outer quadrant of the breast (Fig. 8). Total image time was adjusted to compensate for radioactive decay, with the initial scan acquired for 20 min. Because of the expected increase in secondary (scattered) contamination resulting from the filled torso, a tighter energy window was used to reject scatter. Thus, in these breast+filled torso acquisitions, a symmetric ±4% window about the 140-keV photopeak of Tc-99m was used, providing count rates of ~0.2 kcps.

For the 3-D camera trajectories implemented in these breast+filled torso experiments, the filled torso distal to the breast introduces background activity which is not uniformly in the FOV for each projection angle. Hence, Orlov's criteria is not strictly met. Thus, the primary design goal for the acquisition orbits shifts from meeting Orlov's criterion to maximizing the viewable breast volume. In order to increase the viewable volume, the COR was located as far inside the breast as practicable to image near the chest wall. As a result, these orbits have a minimum polar tilt of 15°, with the exception of tilted-parallel-beam (TPB) which maintains a larger, 45° polar tilt (Table III).

Images were again reconstructed from projection data using the OSEM algorithm with ray-tracing capability, with 8 subsets, 5 iterations, calculated attenuation correction assuming a uniform emission volume, and 2.5-mm grid voxels. A 3-D Hann filter with a cutoff of 0.7 times the Nyquist frequency was applied to the reconstructed data.

Regions of interest (ROIs) were drawn both inside the lesions and circumferentially about each lesion in the breast background. For lesion sizes of 9.5-, 8-, and 5-mm-diameter, ROIs contained 12, 9, and 4 pixels, respectively. In all cases, 24 separate background regions were drawn about each lesion, 8 each in the slice containing the lesion's centroid, in the 2.5-mm slice above, and in the 2.5-mm slice below. The size of the background ROIs drawn about each lesion corresponded to the size of the ROI drawn within that lesion (e.g., for the 9.5-

mm lesion, 24 background regions totaled 288 pixels, whereas for the 8-mm lesion, 24 background regions totaled 216 pixels).

The SNR was measured as the difference in mean pixel values of the lesion and breast background, divided by the standard deviation of the uniform background ($(ROI_{lesion} - ROI_{breast})/\sigma_{breast}$). Lesion contrast is defined as the signal difference divided by the background signal ($(ROI_{lesion} - ROI_{breast})/ROI_{breast}$).

## B. Results

Fig. 9 shows reconstructed results from the 935 ml breast-only measurements, where both lesions are located in the same transaxial plane. Without additional torso contamination, and with a uniform breast background, both the centrally located 8 mm and the proximally located 5-mm-diameter lesions are clearly visible. Table V gives results from calculations of SNR and contrast for both lesions at the second OSEM iteration, smoothed with a Hann filter (which was the optimal tradeoff between gains in contrast and losses in SNR (see [20], [21])).

Fig. 10(a) shows reconstructed results from the 1060 ml breast and filled anthropomorphic torso phantom measurements, for the centrally located 9.5-mm-diameter lesion. Fig. 10(b) shows an example of reconstructed results for the 8-mm lesion. Table V lists results from calculations of SNR and contrast for both the 9.5-mm and 8-mm lesions, again at the second OSEM iteration, smoothed with a Hann filter.

## C. Discussion

The two breast phantoms were chosen for these mammotomography studies because of their similar size (volume), but vastly different shape. The breast's shape was purposely and deliberately altered to examine its effect on the newer orbits evaluated within this work. With a different breast shape, various complications in positioning arise (including ROR control to contour the breast) without significantly changing the amount of scatter, total activity, or attenuation that one might expect with vastly different sized breasts.

In studies with the 935 ml breast, high-count, low-noise images result (Fig. 9). This is not surprising given the fairly large energy window (±8%) and large absolute activity. However, this ideal case does demonstrate the ability of the system to clearly resolve a 5-mm lesion. Furthermore, both subcentimeter diameter lesions were resolved with each improved 3-D sampling scheme, afforded by the flexibility of the hemispherical positioning gantry, suggesting the viability of these trajectories for clinical studies. With the use of a radio-opaque bed to shield the system from additional body background, we are currently investigating whether the image quality, given enough statistics, could ideally resemble that shown in these isolated breast measurements [48].

The TPB orbit (which does not strictly meet Orlov's sufficiency condition) yields the lowest SNR value for the 5-mm lesion. Further, the reconstructed images are riddled with artifacts, including an elongated nipple-chest axis, similar to our previous results [20], [21]. With the more complex orbits that improve volumetric sampling, the breast shape is almost fully recovered. Results also indicate that the orbit most optimal for specific lesion locations may

change; whether this result is more ascribable to the placement of the lesion or the size of the lesion itself is being further investigated.

The viewable breast volume is limited for the 935 ml breast case along the nipple-chest axis. Because the design criteria included meeting Orlov's sampling criteria, the COR was located at the nipple for this particular breast shape and size. Thus, with the lesions optimally placed near the nipple for this set of measurements, resulting images provided for high contrast resolution. However, for lesions located near the chest wall, relatively far from the detector, a COR located at the nipple may preclude their visualization even given improved sampling. Consequently, design criteria for any orbit require a tradeoff between improved sampling and viewable breast volume.

This subsequent optimization of orbit design parameters was examined in the 1060 ml breast + filled torso experiments. The design goal for the orbit implementations for those measurements was to move the COR as far into the breast as practicable. Accordingly, the minimum tilt was increased from 0° to 15° so that the COR could be moved into the breast ~2 cm. This, in turn, increased the viewable breast volume. Indeed, the entire 12-cm length of the nipple-chest wall axis can be seen, as well as some additional depth into the chest wall with only a small missing cone of data behind the chest wall along the nipple-chest axis.

With more realistic uptake ratios in the body and absolute activities of the organs, the 9.5-mm centrally located lesion (~6 cm from the nipple) was discernible in all images. Again, results from the TPB orbit in Fig. 10(a) demonstrate the familiar elongation of the nipple-chest axis. Additionally, increased activity from the background, specifically the liver, is also visible [Fig. 10(a), white arrow]. Interestingly, the remaining orbits, though also incompletely sampling the breast according to Orlov's condition, appear to more nearly recover the breast's shape. This suggests that while the mathematical condition for accurate reconstruction of the activity distribution within the breast was not met, in practice, the sampling requirement may be less strict than initially anticipated; this is an area that warrants further investigation.

Incomplete sampling may, however, produce false positives in the image [Fig. 10(a), CLOVER]; this may also be due to other reconstruction artifacts since these misleading signals are actually manifested as streaks and appear in multiple contiguous planes. The more peripheral areas of the breast along the chest wall may suffer from less sufficient sampling; the uniformity of the sampling scheme itself is currently being investigated in addition to completeness issues.

For this work, there was no patient (torso) shielding whatsoever. Given a radio-opaque support bed, however, background activity should be significantly reduced, as the heart and liver should be removed from a significant number of detector vantages. The shielded bed may also affect the allowed camera trajectories. Our group is in the process of implementing and investigating such a patient bed and its effects (and expected improvements) on image quality [48].

## IV. Conclusion

Dedicated emission mammotomography with a CZT imaging detector that could image large breasts was implemented. Initial characterization and preclinical evaluation studies were performed. The intrinsic characteristics of the medium-FOV, semiconductor imaging detector were evaluated, as was the overall suitability of the device for dedicated SPECT imaging of the breast. The detector was found to have a 6.8% FWHM at 140 keV, and was able to clearly discern 3.1-mm-diameter mini-cold rods in reconstructed images. A key benefit provided by a dedicated, compact SPECT breast imaging system is its ability to acquire fully 3-D molecular data about an *uncompressed*, pendant breast and possibly anterior chest wall. As a potential secondary diagnostic tool, the 3-D sampling scheme can be tailored to an individual patient, especially if mammographic studies can provide *a priori* information about a suspected lesion. Though it appears no single orbit optimizes image quality for lesions at all placements within the breast, the phantom studies shown here demonstrate the capability of the system to easily adapt the acquisition scheme for imaging of various breast shapes and sizes. Additionally, there are no outstanding trajectories that consistently yield optimized quantitative lesion imaging parameters. Qualitatively however, while imaging isolated breasts which are completely in the field-of-view for all vantages yields consistent reconstructed images, imaging breasts with realistic torso backgrounds (out-of-field activity) substantially alters image characteristics and breast morphology. Orbits that improve sampling yield more realistic morphology as well as more accurate overall activity distributions throughout the imaged volumes. Furthermore, results from breast phantom measurements reveal the ability of this approach to visualize lesions <1 cm in diameter, and studies are ongoing to evaluate this ability with vastly different sized breast phantoms [48]. The strength of this molecular imaging approach for breast imaging can be further enhanced with additional structural information provided by transmission cone-beam mammotomography. Initial development of a prototype X-ray computed mammotomograph for such a purpose is underway [30], [31]. The 3-D emission mammotomography system evaluated within this work, incorporating a compact CZT detector, shows a promising, clinically relevant technique for molecular imaging of the whole breast.

## Acknowledgments

This work was supported in part by the National Institutes of Health (NIH) under Grant R01-CA96821 and in part by the U.S. Army under Grant DAMD17-03-1-0558.

The authors thank K. Parnham, J. Li, and B. E. Patt (*Gamma Medica*) for their assistance with camera operation and modification.

## References

1. Khalkhali I, Baum JK, Villaneuva-Meyer J, Edell SL, Hanelin LG, Lugo CE, Taillefer R, Freeman LM, Neal CE, Scheff AM, Connolly JL, Schnitt SJ, Houlihan MJ, Sampalis JS, Haber SB. 99 mTc sestamibi breast imaging for the examination of patients with dense and fatty breasts: Multicenter study. Radiology. 2002; 222:149–155. [PubMed: 11799940]
2. Coover LR, Caravaglia G, Kuhn P. Scintimammography with dedicated breast camera detects and localizes occult carcinoma. J Nucl Med. 2004; 45:553–558. [PubMed: 15073249]

3. Williams MB, Goode AR, Galbis-Reig V, Majewski S, Weisenberger AG, Wojcik R. Performance of a PSPMT based detector for scintimammography. Phys Med Biol. 2000; 45:781–800. [PubMed: 10730971]
4. Majewski S, Kieper D, Curran E, Keppel C, Kross B, Palumbo A, Popov V, Weisenberger AG, Welch B, Wojcik R, Williams MB, Goode AR, More M, Zhang G. Optimization of dedicated scintimammography procedure using detector prototypes and compressible phantoms. IEEE Trans Nucl Sci. Jun; 2001 48(3):822–829.
5. Kim J, Choi Y, Joo K, Sihn B, Chong J, Kim SE, Lee KH, Choe YS, Kim B. Development of a miniature scintillation camera using an NaI(Tl) scintillator and PSPMT for scintimammography. Phys Med Biol. 2000; 45:3481–3488. [PubMed: 11098918]
6. McElroy DP, Hoffman EJ, MacDonald L, Patt BE, Iwanczyk JS, Yamaguchi Y, Levin CS. Evaluation of breast tumor detectability with two dedicated, compact scintillation cameras. IEEE Trans Nucl Sci. Jun; 2002 49(3):794–802.
7. Buscombe JR, Cwikla JB, Holloway B, Hilson AJW. Prediction of the usefulness of combined mammography and scintimammography in suspected breast cancer using ROC curves. J Nucl Med. 2001; 42:3–8. [PubMed: 11197976]
8. Spanu A, Dettori G, Nuvoli S, Porcu A, Falchi A, Cottu P, Solinas ME, Scanu AM, Chessa F, Madeddu G. 99 mTc-Tetrofosmin SPET in the detection of both primary breast cancer and axillary lymph node metastasis. Eur J Nucl Med. 2001; 28:1781–1794. [PubMed: 11734916]
9. Fahey FH, Grow KL, Weber RL, Harkness BA, Bayram E, Hemler PH. Emission tuned-aperture computed tomography: A novel approach to scintimammography. J Nucl Med. 2001; 42:1121–1127. [PubMed: 11438637]
10. Seret A, Defrise M, Blocklet D. 180-degree pinhole SPET with a tilted detector and OS-EM reconstruction: Phantom studies and potential clinical applications. Eur J Nucl Med. 2001; 28:1836–1841. [PubMed: 11734923]
11. Spanu A, Dettori G, Chiaramida P, Cottu P, Falchi A, Porcu A, Solinas ME, Nuvoli S, Madeddu G. The role of 99 mTc-tetrofosmin pinhole SPECT in breast cancer axillary lymph node staging. Cancer Biother Radiopharm. 2000; 15:81–91. [PubMed: 10740656]
12. Scarfone C, Jaszczak RJ, Li J, Soo MS, Smith MF, Greer KL, Coleman RE. Breast tumor imaging using incomplete orbit pinhole SPET: A phantom study. Nucl Med Commun. 1997; 18:18:1077–18:1086.
13. Wang H, Scarfone C, Greer KL, Coleman RE, Jaszczak RJ. Prone breast tumor imaging using vertical axis-of-rotation (VAOR) SPECT systems: An initial study. IEEE Trans Nucl Sci. Jun; 1997 44(3):1271–1276.
14. Pieper BC, Bowsher JE, Tornai MP, Peter J, Jaszczak RJ. Breast tumor imaging using tiltable head SPECT camera. IEEE Trans Nucl Sci. Aug; 2001 48(4):1477–1492.
15. Tornai MP, Bowsher JE, Jaszczak RJ, Pieper BC, Greer KL, Hardenbergh PH, Coleman RE. Mammotomography with pinhole incomplete circular orbit SPECT. J Nucl Med. 2003; 44:585–593.
16. Bowsher JE, Tornai MP, Metzler SD, Peter J, Jaszczak RJ. SPECT breast imaging using more nearly complete orbits and combined pinhole-parallel-beam collimation. IEEE Nucl Sci Symp Conf Rec. Nov.2001 3:1328–1330.
17. Metzler SD, Bowsher JE, Tornai MP, Pieper BC, Peter J, Jaszczak RJ. SPECT breast imaging combining horizontal and vertical axes of rotation. IEEE Trans Nucl Sci. Feb; 2002 49(1):31–36.
18. Tornai MP, Archer CN, Bowsher JE, Patt BE, Iwanczyk JS, MacDonald LR, Parnham K. Feasibility of full-field single photon emission mammotomography using a novel CZT detector. IEEE Nucl Sci Symp Conf Rec. Nov.2002 3:1901.
19. Pani R, Soluri A, Scafe R, Pellegrini R, de Vincentis G, Cinti MN, Betti M, Inches R, Garibaldi G, Cusanno F, Gambaccini M, Fantini A, Taibi A, Olivo A, Pani S, Rigon L, Bollini D, Lanconelli N, Del Guerra A. Feasibility study for SPECT mammography based on compact imagers rotating around breast vertical axis. IEEE Nucl Sci Symp Conf Rec. Nov.2000 3:21/36–21/39.
20. Tornai MP, Bowsher JE, Archer CN, Peter J, Jaszczak RJ, MacDonald LR, Patt BE, Iwanczyk JS. A 3-D gantry single photon emission tomograph with hemispherical coverage for dedicated breast imaging. Nucl Inst Meth. 2003; A497(1):157–167.

21. Archer CN, Tornai MP, Bowsher JE, Metzler SD, Pieper BC, Jaszczak RJ. Implementation and initial characterization of acquisition orbits with a dedicated emission mammotomograph. IEEE Trans Nucl Sci. Jun; 2003 50(3):418–420.
22. Singh M, Mumcuoglu E. Design of a CZT based BreastSPECT system. IEEE Trans Nucl Sci. Jun; 1998 45(3):1158–1165.
23. Mueller B, O'Conner MK, Blevis I, Rhodes DJ, Smith R, Collins DA, Phillips SW. Evaluation of a small cadmium zinc telluride detector for scintimammography. J Nucl Med. 2003; 44:602–609. [PubMed: 12679406]
24. Butler JF, Lingren CL, Friesenhahn SJ, Doty FP, Ashburn WL, Conwell RL, Augustine FL, Apotovsky B, Pi B, Collins T, Zhao S, Isaacson C. CdZnTe solid-state gamma camera. IEEE Trans Nucl Sci. Jun; 1998 45(3):359–363.
25. Eisen Y, Mardor I, Shor A, Baum Z, Bar D, Feldman G, Cohen H, Issac E, Haham-Zada R, Blitz S, Cohen Y, Glick B, Falk R, Roudebush S, Blevis I. NUCAM3—A gamma camera based on segmented monolithic CdZnTe detectors. IEEE Trans Nucl Sci. Aug; 2002 49(4):1728–1732.
26. Zeng GL, Gagnon D. CdZnTe strip detector SPECT imaging with a slit collimator. Phys Med Biol. 2004; 49:2257–2271. [PubMed: 15248576]
27. Marks DG, Barber HB, Barrett HH, Dereniak EL, Eskin JD, Matherson KJ, Oolfenden JM, Young ET, Augustine FL, Hamilton WJ, Venzon JE, Apotovsky BA, Doty FP. A 48 × 48 CdZnTe array with multiplexer readout. IEEE Trans Nucl Sci. Jun; 1996 43(3):1253–1259.
28. Verger L, Gentet MC, Gerfault L, Guillemaud R, Mestais C, Monnet O, Montemont G, Petroz G, Rostaing JP, Rustique J. Performance and perspectives of a CdZnTe-based gamma camera for medical imaging. IEEE Trans Nucl Sci. Dec; 2004 51(6):3111–3117.
29. Williams MB, Narayanan D, More MJ, Goodale PJ, Majewski S, Kieper DA. Analysis of position-dependent Compton scatter in scintimammography with mild compression. IEEE Trans Nucl Sci. Oct; 2003 50(5):1643–1649.
30. McKinley RL, Samei E, Brzymialkiewicz CN, Tornai MP, Floyd CE. Measurements of an optimized beam for x-ray computed mammotomography. Proc SPIE (Phys Med Imag). 2004; 5368:311–319.
31. Tornai MP, McKinley RL, Brzymialkiewicz CN, Madhav P, Cutler SJ, Crotty DJ, Bowsher JE, Samei E, Floyd CE. Design and development of a fully-3D dedicated X-ray computed mammotomographic system. Proc SPIE (Physics of Medical Imaging). 2005; 5745(1):189–197.
32. Orlov SS. Theory of three dimensional reconstruction. Sov Phys Crystallogr. 1975; 20(3):312–314.
33. Metzler SD, Bowsher JE, Jaszczak RJ. Geometrical similarities of the Orlov and Tuy sampling criteria and a numerical algorithm for assessing sampling completeness. IEEE Trans Nucl Sci. Oct; 2003 50(5):1550–1555.
34. Cherry SR, Sorenson JA, Phelps ME. Physics in Nuclear Medicine. 2003:227–251.
35. Anger, HO. Radioisotope cameras. In: Hine, GJ., editor. Instrumentation in Nuclear Medicine. Vol. 1. New York, NY: Academic; 1967. p. 485-552.
36. Hudson HM, Larkin RS. Accelerated image reconstruction using ordered subsets of projection data. IEEE Trans Med Imag. Dec; 1994 13(4):601–609.
37. Bowsher JE, Gilland DR, Floyd CE, Jaszczak RJ, Johnson VE, Coleman RE. Three dimensional iterative reconstruction for SPECT. J Nucl Med. 1992; 33:879. abstract.
38. Performance Measurements of Scintillation Cameras. EMA Standards Publication; NU 1-2001
39. Gunter, D.; Matthews, K., II; Ordõnez, C. The interaction of collimator lattice periodicity and detector pixelation. IEEE Nucl. Sci. Symp. Conf. Rec.; Nov. 1998; p. 1525-1531.
40. Jeanguillaume, C.; Douiri, A.; Quartuccio, M.; Begot, S.; Franck, D.; Tence, M.; Ballongue, P. CACAO a collimation means well suited for pixellated γ-camera. IEEE Nucl. Sci. Symp. Conf. Rec.; Nov. 2001; p. 2291-2294.
41. Smith MF, Majewski S, Weisenberger AG. Optimizing pinhole and parallel hole collimation for scintimammography with compact pixellated detectors. IEEE Trans Nucl Sci. Jun; 2003 50(3): 321–326.
42. Kalinosky, MA.; Wagenaar, DJ.; Pawlak, J.; Rempel, T.; Engdahl, JC. Aliasing in pixellated detectors. Proc. Future Directions in Nuclear Medicine Physics and Engineering; 1999; p. 41

43. Tuy HK. An inversion formula for cone-beam reconstruction. SIAM J Appl Math. 1983; 43:546–552.

44. Scopinaro F, Pani R, De Vincentis G, Soluri A, Pellegrini R, Porfiri L. High-resolution scintimammography improves the accuracy of technetium-99m methoxyisobutylisonitrile scintimammography: Use of a new dedicated gamma camera. Eur J Nucl Med. 1999; 26:1279–1288. [PubMed: 10541826]

45. Maublant J, de Latour M, Mestas D, Clemenson A, Charrier S, Feillel V, Le Bouedec G, Kaufmann P, Dauplat J, Veyre A. Technetium-99m-sestamibi uptake in breast tumor and associated lymph nodes. J Nucl Med. 1996; 37(6):922–925. [PubMed: 8683312]

46. Pani R, De Vincentis G, Scopinaro F, Pellegrini R, Soluri A, Weinberg IN, Pergola A, Scafe R, Trotta G. Dedicated gamma camera for single photon emission mammography (SPEM). IEEE Trans Nucl Sci. Dec; 1998 45(6):3127–3133.

47. ThWackers FJ, Berman DS, Maddahi J, Watson DD, Beller GA, Strauss HW, Boucher CA, Picard M, Holman BL, Fridrich R, Inglese E, Delaloye B, Bischof-Delaloye A, Camin L, McKusick K. Technetium-99m hexakis 2-methoxyisobutyl isonitrile: Human biodistribution, dosimetry, safety, and preliminary comparison to thallium-201 for myocardial perfusion imaging. J Nucl Med. 1989; 30(3):301–311. [PubMed: 2525610]

48. Brzymialkiewicz, CN.; Tornai, MP.; McKinley, RL.; Bowsher, JE. 3-D data acquisition sampling strategies for dedicated emission mammotomography for various breast sizes. presented at the 2004 IEEE Nucl. Sci. Symp. and Med. Imag. Conf.; Rome, Italy. Oct. 16–22, 2004;

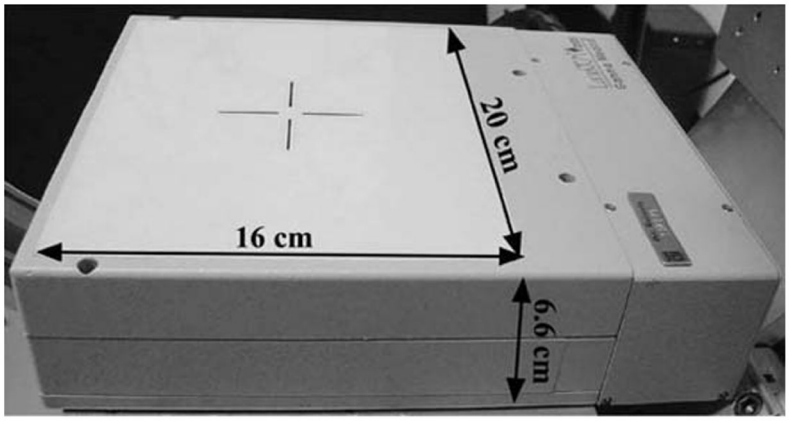


**Fig. 1.**
Photograph of the compact CZT detector with 16 × 20 $cm^2$ field of view (FOV).

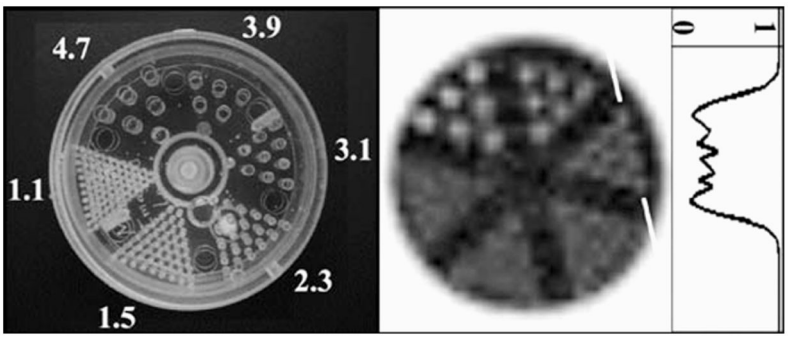


**Fig. 2.**

(Left) Photograph of the mini-rod phantom, with diameters labeled (in mm), with a pitch equal to twice their diameter. (Middle) OSEM reconstructed mini-rod data (8 subsets, 20 iterations, 2.5-mm voxels, 5 summed slices to reduce noise, correction for COR partial pixel shift) acquired with 4.4-cm ROR. (Right) Profile (one-pixel wide) drawn through the 3.1-mm rods at edge, as indicated. Darker grayscale values indicate areas where activity is present (normalized to 1 in this case); white areas (i.e., the rods) are cold.

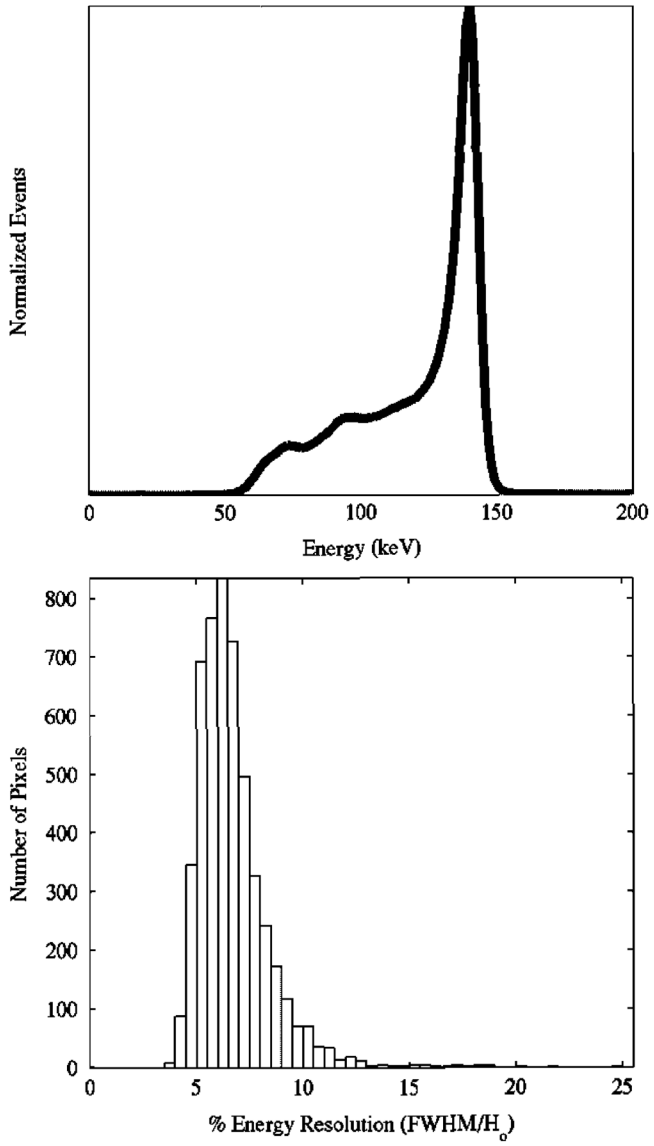


**Fig. 3.**

(Top) Gain balanced, summed energy spectra of all active pixels. As per NEMA-2001 specifications, the measured FWHM energy resolution was 6.8%. (Bottom) Histogram of FWHM Energy Resolutions for all discrete pixels. Mean = 6.7%; Median = 6.4%; Min = 3.5%; Max = 24.8%.

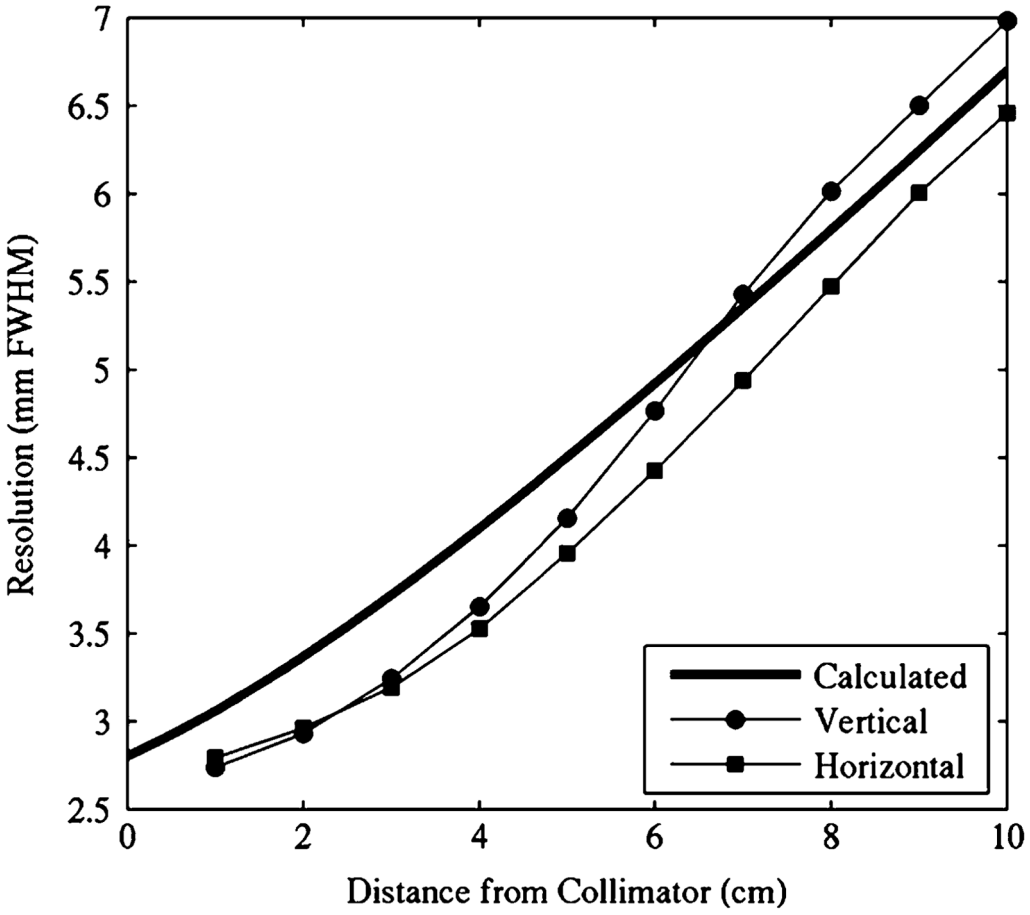


**Fig. 4.**

Planar spatial resolution results from capillary line source measurements match calculated values.

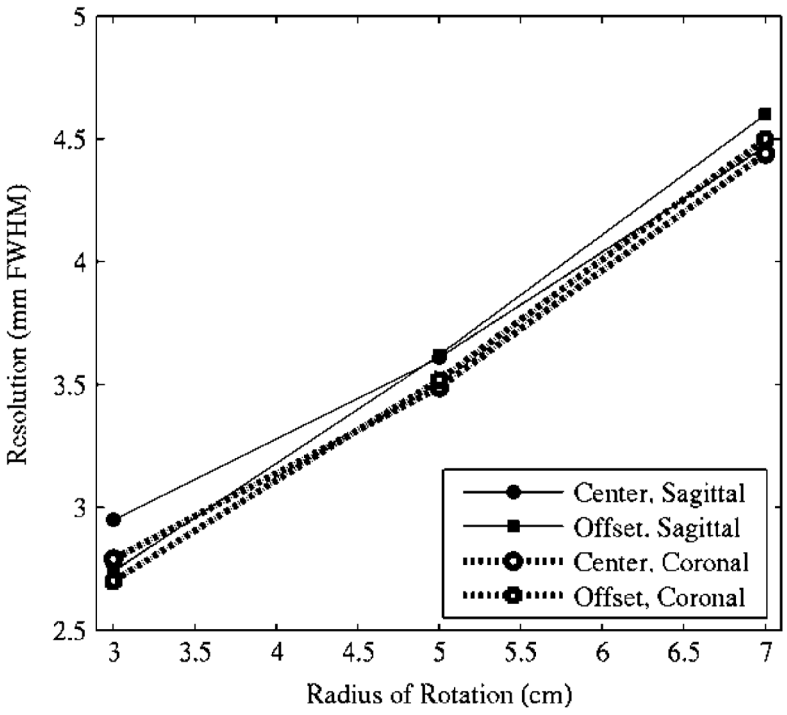


**Fig. 5.**

Reconstructed SPECT spatial resolution results measured through two capillary tubes located at the ROR center and 2-cm offset. Data obtained from 10-pixel-wide profiles drawn in both the coronal and sagittal slices from the fifth iteration of the reconstructed data.

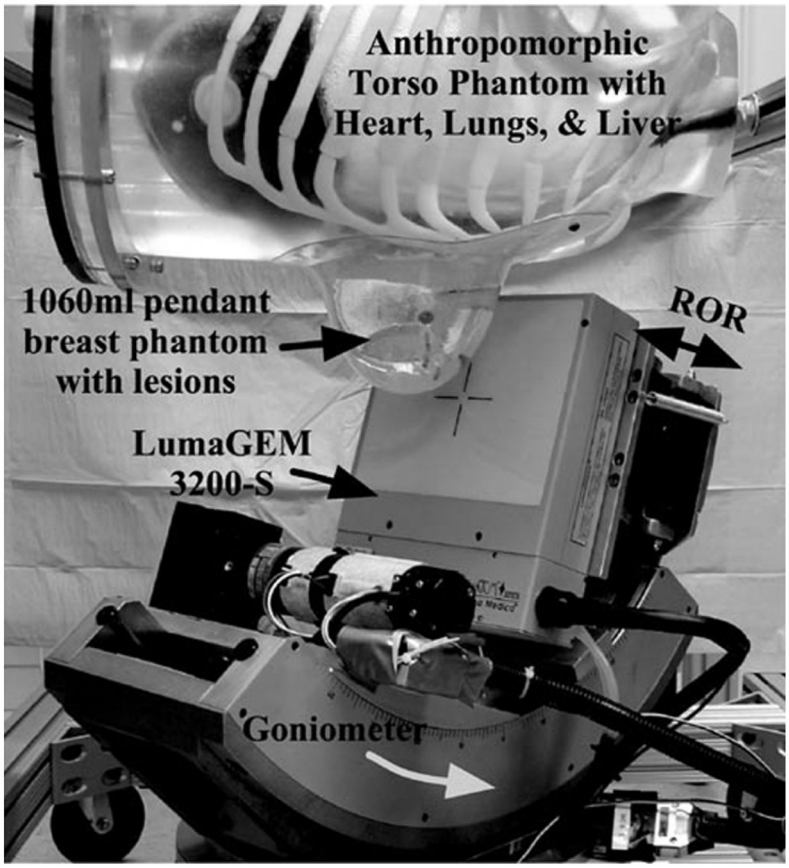


**Fig. 6.**

Dedicated emission mammotomography system with camera mounted on the hemispherical positioning gantry. A filled anthropomorphic torso phantom and pendant, uncompressed 1060 ml breast are suspended within the camera's FOV.

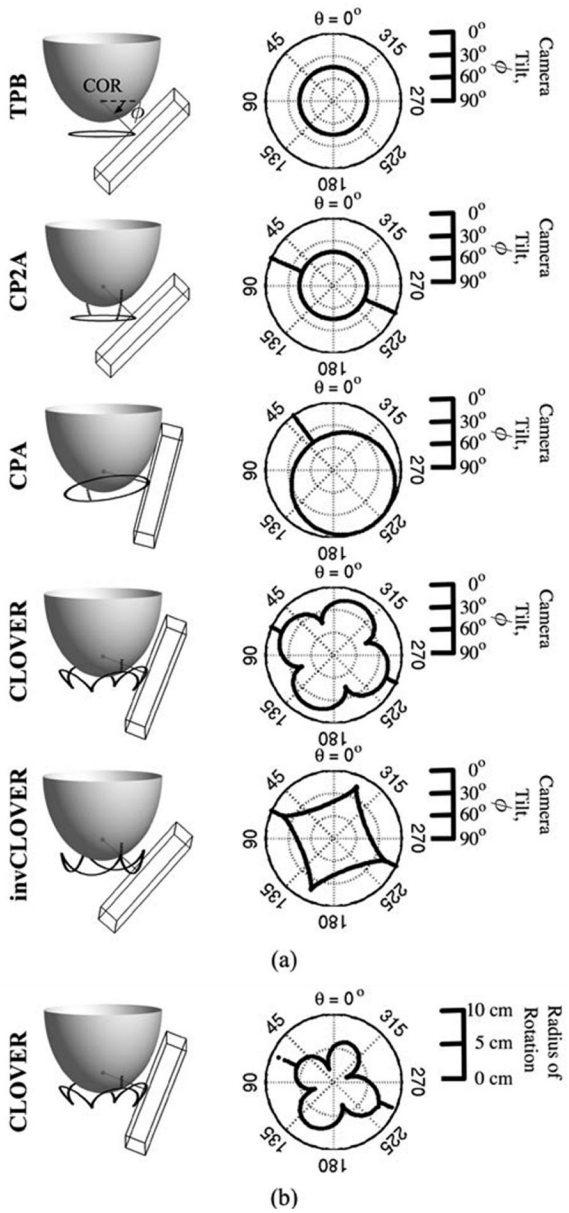


**Fig. 7.**

(a) Scale schematics of orbits, with 1060 ml breast modeled. The wire-frame box represents the 16 × 20 $cm^2$ active detector FOV, with center on the trajectory (black orbit path) about the breast. Orbits are (Top to Bottom): Tilted-Parallel-Beam (TPB); Circle-Plus-Two-Arcs (CP2A); Circle-Plus-Arc (CPA); Cloverleaf (CLOVER); and Inverse Cloverleaf (invCLOVER) (see, also, Table III). Labeled in TPB schematic are the: center of rotation (COR), located ~2 cm inside the breast along the nipple-chest axis; direction of increased polar camera tilt (small arrow). Dark gray line from COR is perpendicular to the detector face. Note that while these implementations meet Orlov's criteria for sufficient sampling, simple modifications allow for more viewable breast volume when physical hindrances preclude sufficient sampling. Next to each 3-D schematic are polar plots of camera polar tilt ($\varphi$) (plotted as a radius, with 90° at center and 0° at edge) versus azimuthal angle ($\theta$) (plotted

around the circle from 0° to 360°). (b) For CLOVER orbit, example polar plot of ROR contouring (0 cm radius at center), which allows camera to move close to the breast, as a function of azimuthal angle ($\theta$).

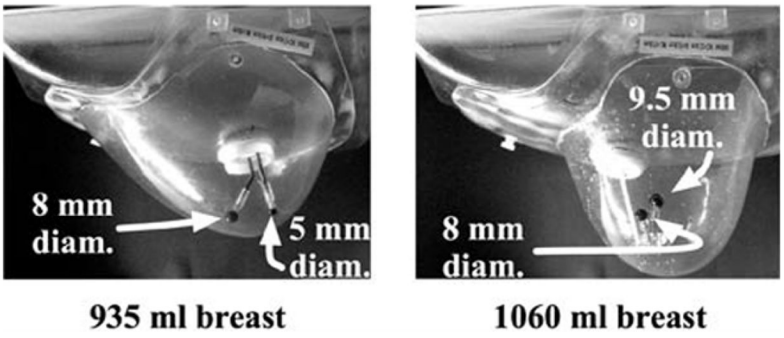


**Fig. 8.**

Photographs of the (left) 935 ml and (right) 1060 ml anthropomorphic breast phantoms. Dimensions of both phantoms are given in Table II. Two sets of embedded lesions were inserted into each phantom as shown.

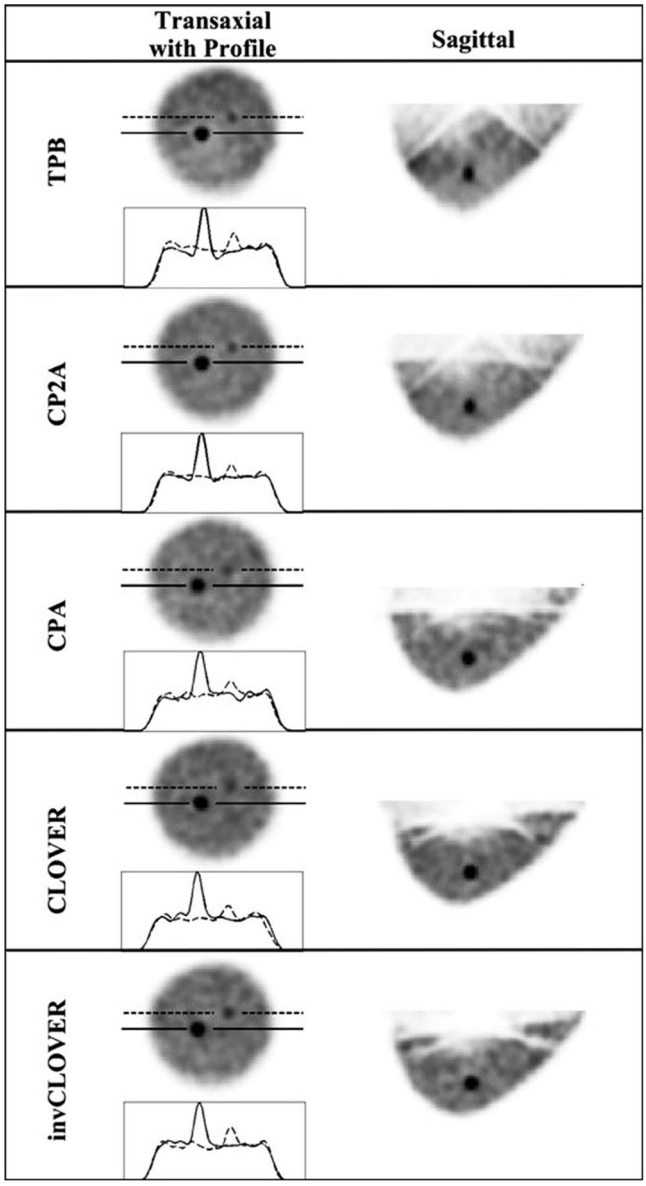


**Fig. 9.**

OSEM reconstructed data (8 subsets, second iteration smoothed with Hann filter shown) from the 935 ml breast data, for each labeled orbit, with a 9.8:1 lesion:breast radionuclide concentration ratio. Solid line in transaxial slice and profile is through the 8-mm lesion, and the dashed line is through the 5-mm lesion. Note that incomplete sampling artifacts from reconstructed data seen with the TPB orbit sagittal views are reduced with the more complex orbits that improve sampling, similar to results shown in [20] and [21].

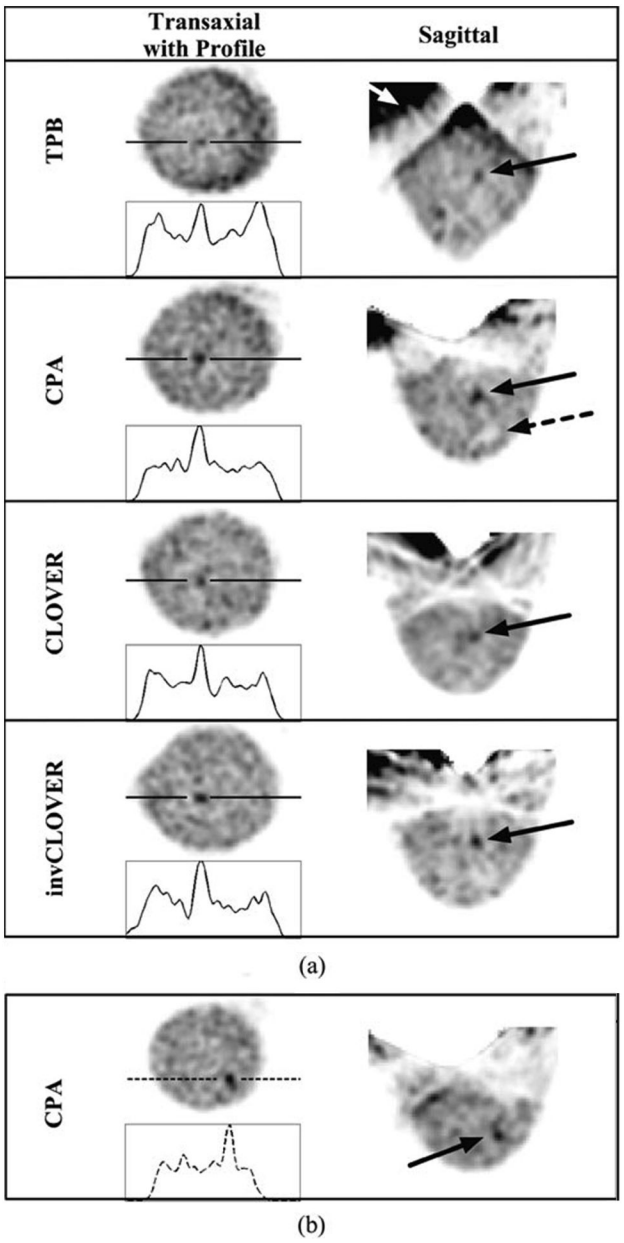


**Fig. 10.**

OSEM reconstructed data (8 subsets, second iteration smoothed with Hann filter shown) from the 1060 ml breast + filled torso data, for each labeled orbit with an incomplete sampling scheme, with a 6.1:1:12 lesion:breast-and-torso:liver-and-heart radionuclide concentration ratio. (a) Solid line is drawn through the 9.5-mm lesion. Note the increased background contamination with TPB (white arrow) as compared to the other orbits which do not maintain the large detector polar tilts, thus limiting more direct views of the heart and liver. Even with these incompletely sampled orbits, and more realistic absolute radioactivities within the phantom, the centrally located 9.5-mm lesion is clearly visible. Dashed arrow in CPA points to cold lesion holder, which can also be seen with the other

orbits (see, also, InvCLOVER) and in Fig. 8. (b) Views of the 8-mm lesion at different transaxial and sagittal locations than the larger lesion.

**TABLE I**

Average Planar Spatial Resolution FWHM and FWTM as Per [38]

| | Direction Along Detector | | | |
|---|---|---|---|---|
| | Horizontal | | Vertical | |
| Collimator-Source Distance (cm) | FWHM (mm) | FWTM (mm) | FWHM (mm) | FWTM (mm) |
| 1 | 3.4 ± 0.7 | 6.3 ± 0.7 | 3.7 ± 0.7 | 6.6 ± 0.4 |
| 10 | 6.7 ± 0.1 | 12.2 ± 0.3 | 7.3 ± 0.2 | 13.0 ± 0.3 |

**TABLE II**

Dimensions of the Custom Breast Phantoms

| Breast Volume (ml) | Dimensions (in cm) | | |
|---|---|---|---|
| | Superior-Inferior | Nipple-Chest | Medial-Lateral |
| 935 | 20 | 7.5 | 15 |
| 1060 | 16 | 12 | 18 |

## TABLE III

Orbit Parameters Used for Each Breast Phantom Acquisition, With All Orbits Acquired Over a 360° Azimuthal Range ($\theta$)

| Orbit Name | Acronym | $\varphi$ Range (min-max) (degrees) | ROR Range (min-max) (cm) | Number of Prjs |
|---|---|---|---|---|
| *935 ml Breast, COR located at nipple* | | | | |
| Tilted-Parallel-Beam | TPB | 45° | 1.9 – 3.7 | 128 |
| Circle-Plus-Two-Arcs | CP2A | 0 – 45° | 1.9 – 9.3 | 162 |
| Circle-Plus-Arc | CPA | 0 – 45° | 2.4 – 9.3 | 145 |
| Cloverleaf | CLOVER | 0 – 45° | 2.0 – 9.3 | 268 |
| Inverse Cloverleaf | invCLOVER | 0 – 45° | 2.0 – 9.3 | 268 |
| *1060 ml Breast + Filled Torso, COR located ~2 cm inside nipple* | | | | |
| Tilted-Parallel-Beam | TPB | 45° | 3.2 – 4.4 | 128 |
| Circle-Plus-Arc | CPA | 15 – 45° | 3.8 – 7.1 | 139 |
| Cloverleaf | CLOVER | 15 – 45° | 3.6 – 7.2 | 256 |
| Inverse Cloverleaf | invCLOVER | 15 – 45° | 3.6 – 7.1 | 256 |

**TABLE IV**

Activity Concentration Ratios for Each of the Filled Organs in the Anthropomorphic Torso and Breast Phantoms

| Organ | Volume (ml) | Concentration ($\mu$Ci/ml) | Ratio |
|---|---|---|---|
| Breast | 1060 | 0.33 | 1.0 |
| Torso | 7810 | 0.33 | 1.0 |
| Liver | 1010 | 4.2 | 12.7 |
| Heart (outer wall) | 290 | 4.0 | 12.1 |
| 9.5 mm diam. lesion | 0.43 | 2.0 | 6.1 |
| 8.0 mm diam. lesion | 0.26 | 2.0 | 6.1 |

**TABLE V**

Measured SNRs and Contrasts, at 2nd OSEM Iteration, Smoothed With a Hann Filter

| | Lesion Size | | | | | |
|---|---|---|---|---|---|---|
| | 9.5 mm (0.43 ml) | | 8 mm (0.26 ml) | | 5 mm (0.06 ml) | |
| **Orbit** | **SNR** | **Contrast** | **SNR** | **Contrast** | **SNR** | **Contrast** |
| *Ideal low-noise case with high uptake:*<br>*935 ml Breast Only*<br>*10:1 activity concentration ratio, 12.1 μCi/ml in lesions, 16% EWin* | | | | | | |
| | | | central | | distal | |
| TPB | – | – | 19.3 | 2.0 | 2.7 | 0.2 |
| CP2A | – | – | 26.6 | 1.9 | 4.9 | 0.2 |
| CPA | – | – | 17.3 | 1.4 | 3.9 | 0.2 |
| CLOVER | – | – | 23.2 | 1.4 | 7.9 | 0.3 |
| invCLOVER | – | – | 17.1 | 1.5 | 6.9 | 0.3 |
| *More realistic case simulating patient biology:*<br>*1060 ml Breast + Filled Torso,*<br>*6.1:1:12 activity concentration ratio, 2.0 μCi/ml in lesions, 8% EWin* | | | | | | |
| | central | | distal | | | |
| TPB | 4.6 | 0.8 | 3.4 | 0.5 | – | – |
| CPA | 4.8 | 1.0 | 5.5 | 0.6 | – | – |
| CLOVER | 3.7 | 0.8 | 2.0 | 0.3 | – | – |
| invCLOVER | 6.3 | 1.2 | 1.2 | 0.2 | – | – |